

Optical Detection and Manipulation of Pseudospin Orders in Wigner Crystals

Yichen Dong¹, Eugene Demler^{2,†}, and Zhiyuan Sun^{1,3,*}

¹State Key Laboratory of Low-Dimensional Quantum Physics and Department of Physics, Tsinghua University, Beijing 100084, P. R. China

²Institute for Theoretical Physics, ETH Zurich, 8093 Zurich, Switzerland

³Frontier Science Center for Quantum Information, Beijing 100084, P. R. China

(Dated: December 25, 2025)

In Wigner-crystal states of two-dimensional electrons, the spin ordering remains poorly understood. The small energy differences between candidate spin orders make theoretical studies less reliable, and probing magnetic order at a nonzero wave vector is experimentally challenging. In modern realizations of Wigner crystals, the electronic spin degree of freedom is often replaced by a valley pseudospin associated with nonzero Berry curvature. The resulting anomalous velocity couples the electrons' pseudospin texture to their orbital vibration. We show that this mechanism enables optical detection of pseudospin orders in Wigner crystals by producing sharp signatures in the terahertz optical conductivity. For example, antiferromagnetic pseudospin order enables light to excite collective electronic vibrations at the ordering wave vector, generating a characteristic absorption peak. Based on the same principle, we further show that a strong optical drive generates an effective potential that reshapes the pseudospin energy landscape, inducing phase transitions to stripe antiferromagnetic states. These results point to a route for optical detection and control of spin order via its coupling to orbital motion.

Introduction—Wigner predicted in 1934 that at low densities, electrons are driven by Coulomb interaction to form a crystal [1–3]. Signatures of two dimensional (2D) Wigner crystals were observed later with [4] and without [5, 6] magnetic fields. Recently, Wigner crystals have seen an experimental revival due to the emergence of 2D transition metal dichalcogenides (TMDCs) [3, 7–10], graphene [11] and their moiré structures [12, 13]. Remarkably, people are now able to directly image 2D Wigner crystals with scanning tunneling microscopy [10, 11, 13].

On top of the Wigner lattice, the electronic spin structure has been theoretically predicted to exhibit a rich phase diagram [14–21] but remains experimentally mysterious [9, 22, 23]. Moreover, the modern host materials such as 2D TMDCs [7–10, 16, 18, 24], their moiré bilayers [12, 13], and rhombohedral multilayer graphene [25–30] introduce valley-pseudospin degrees of freedom to the electrons/holes [31–33], raising intriguing questions of possible pseudospin orders [18] in Wigner crystals. Unfortunately, because of the weak coupling of pseudospin orders, especially antiferromagnetic ones, to conventional transport and imaging techniques, their experimental study is limited.

In this work, we present a theoretical framework to demonstrate that the valley-pseudospin order in Wigner crystals can be both detected and manipulated using terahertz (THz) optics. This is because the valley-pseudospin is associated with Berry curvature, so that it couples to the orbital motion of the electron via the anomalous velocity [31, 34, 35]. As a result, the spatial pseudospin order at momentum q couples the incident light to the electronic phonons at the same momentum, which are otherwise dark. This in turn contributes resonance peaks to the optical conductivity spectrum at the corresponding phononic frequencies. We further show that, because of the same reason, a strong optical driving field will generate an effective ponderomotive potential [36] that modifies the pseudospin energy landscape in the nonequilibrium regime. The ponderomotive potential drives phase transitions from ferro-

magnetic into stripe antiferromagnetic (AFM) states, with the ordering wave vector tunable by the pump frequency.

The Model—The phase-space Lagrangian of a Wigner crystal driven by light can be written as [34]

$$L_{\text{f}} = \sum_i \left(-\mathbf{k}_i \cdot \dot{\mathbf{u}}_i + \frac{\mathbf{k}_i^2}{2m} - \mathbf{A}(\mathbf{k}_i, \mathbf{S}_i) \cdot \dot{\mathbf{k}}_i \right) + \sum_{ij} \mathbf{u}_i \hat{\phi}_{ij} \mathbf{u}_j - \mathbf{E}(t) \cdot \mathbf{P}[u] \quad (1)$$

where \mathbf{k}_i and \mathbf{u}_i represent the momentum and displacement of the i th localized electron in the lattice and we have set the Planck constant \hbar to unity. We have focused on the case of one electron per unit cell. The first line describes the lattice vibrations of electrons with anomalous velocity corrections, where $\mathbf{A}(\mathbf{k}_i, \mathbf{S}_i)$ is the Berry connection of the i th electron in momentum space. In 2D with nearly constant Berry curvature $\Omega_i = \Omega S_i^z$ associated to the pseudospin S_i^z , such as the valley pseudospin of low density carriers in TMDCs [31, 34] and their moiré bilayers, one may write

$$\mathbf{A}(\mathbf{k}_i, \mathbf{S}_i) = \Omega_i k_i^x \hat{y} = \Omega S_i^z k_i^x \hat{y}. \quad (2)$$

Note that although we are dealing with pseudospin $1/2$, the maximum values of S_i^z are ± 1 in our notation. The $\hat{\phi}$ is the long range Coulomb potential kernel between the electronic displacements that gives rise to the spring constants for phonons. The incident uniform light couples to matter via its dynamical electric field coupled to the total change of polarization $\mathbf{P}[u] = e \sum_i \mathbf{u}_i$.

The Hamilton's least-action principle in the phase space ($\delta S / \delta k = \delta S / \delta u = 0$ where $S[k, u] = \int dt L_{\text{f}}$ is the action) yields the well known equations of motion with anomalous velocity correction: $\dot{\mathbf{u}}_i = \mathbf{k}_i / m + \dot{\mathbf{k}}_i \times (\Omega_i \hat{z})$, $\dot{\mathbf{k}}_i = -\partial_{\mathbf{u}_i} U$ where U is the potential that includes the last two terms of Eq. (1). After eliminating the momenta k_i and introducing the reduced electric field $\mathcal{E} = e\mathbf{E}/m$ and Berry curvature $\hat{g}_i = m\Omega_i \hat{e}$ where $\hat{e} = \begin{pmatrix} 0 & 1 \\ -1 & 0 \end{pmatrix}$ is the antisymmetric tensor,

the equation of motion for the lattice displacements reads

$$\ddot{\mathbf{u}}_i = (1 - \hat{g}_i \partial_t) \left(- \sum_j \hat{\phi}_{ij} \mathbf{u}_j + \mathcal{E} \right). \quad (3)$$

Eq. (3) describes the dynamics of collective electronic vibrations in the presence of a static valley-pseudospin texture. The latter affects the vibration dynamics via the \hat{g}_i term that introduces valley-pseudospin-dependent anomalous velocities. In the absence of the driving field and the Berry curvature terms, Eq. (3) renders the bare phonon modes of the Wigner crystal whose dispersion is shown in Fig. 1(b). In the following, we define $\omega_{\alpha,q}$ and $\tilde{v}_{\alpha,q} = \mathbf{v}_{\alpha,q} e^{i\mathbf{q}\cdot\mathbf{R}}$ as the frequency and normal coordinate of the phonon mode of branch α at momentum q satisfying $|\mathbf{v}_{\alpha,q}|^2 = 1$. In the 2D Wigner crystal, $\alpha = L$ corresponds to the longitudinal mode (red curve in Fig. 1(b)) and $\alpha = T$ corresponds to the transverse mode (blue curve). In the long wavelength limit, the longitudinal mode (red curve) is just the plasmon with the dispersion $\omega_{L,q} = \sqrt{2q\pi n e^2/m}$ where $n = 2/(\sqrt{3}a^2)$ is the carrier density and a is the lattice constant.

For later convenience, we quantify the pseudospin structure through the correlation function between their z components

$$\chi_{ij} = \langle S_i^z S_j^z \rangle, \quad \chi_q = \frac{1}{N} \sum_j e^{-i\mathbf{q}\cdot(\mathbf{R}_i - \mathbf{R}_j)} \chi_{ij} \quad (4)$$

where \mathbf{R}_i is the spatial coordinate of the i -th lattice site, N is the total number of sites, and $\langle \dots \rangle$ means ensemble average. Defining the momentum- q component of the z -pseudospins as $S_q^z = \frac{1}{N} \sum_i e^{-i\mathbf{q}\cdot\mathbf{R}_i} S_i^z$, one has $\chi_q = \langle S_{-q}^z S_q^z \rangle$ which directly reflects the spatial ordering of z -pseudospins at wave vector q . A delta function structure of χ_q at momentum q_0 indicates long-range pseudospin order at this momentum. We note that if the pseudospins are along S^x or S^y directions, the anomalous velocity stretches the electron's wave packet instead of shifting its center of mass. This quantum mechanical effect is not included in Eq. (1) and will be addressed in the Discussion section.

Optical Detection— We now investigate the linear response of the Wigner crystal to a probing electric field $\mathcal{E}(t) = \mathcal{E} e^{-i\omega t}$ with Eq. (3). We will show that the valley-pseudospin order has characteristic signatures as peaks in the optical conductivity. Formally, the solution can be expressed as

$$\mathbf{u} = [\hat{G}^{-1}(\omega) + i\omega \hat{g} \hat{\phi}]^{-1} (1 + i\omega \hat{g}) \mathcal{E} \quad (5)$$

where the lattice indices are absorbed in \mathbf{u} , \hat{g} and $\hat{\phi}$, and $\hat{G}(\omega) = (\hat{\phi} - \omega^2)^{-1}$ is the bare retarded Green function of the lattice to the driving field. The Green function has the property $\hat{G}(\omega) \tilde{v}_{\alpha,q} = (\omega_{\alpha,q}^2 - \omega^2)^{-1} \tilde{v}_{\alpha,q}$.

In the limit of zero Berry curvature (\hat{g}), the equation of motion Eq. (3) exhibits Galilean invariance under uniform external field. In other words, all electrons are driven by the external field to move in phase with the same displacement, so that the driven dynamics is purely that of the center of mass of the whole crystal, while the internal structure of the crystal

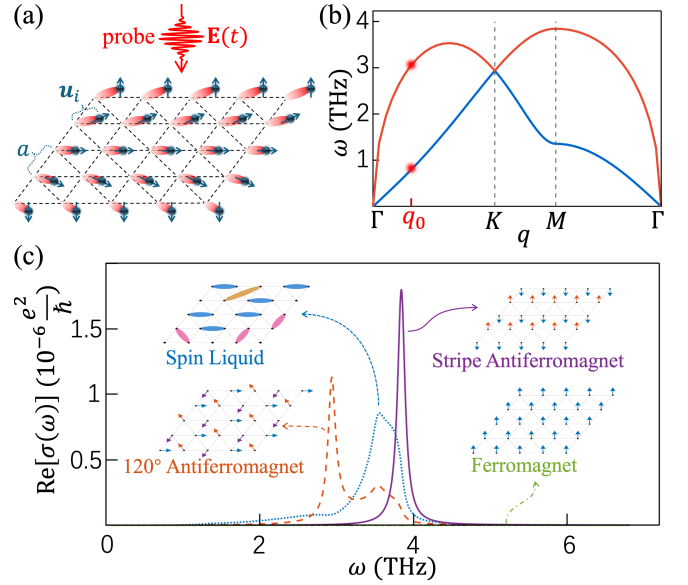


FIG. 1. Optical detection of the pseudospin order. (a) Schematic of the electronic displacements in a triangular-lattice Wigner crystal driven by a dynamical uniform electric field. Because of the different anomalous velocities associated with different pseudospins, the forced motion of the electrons are not uniform, which distorts the lattice. (b) Its phonon dispersion in the limit of zero Berry curvature. (c) The real part $\sigma_1(\omega)$ of the optical conductivities of a Wigner crystal for different pseudospin configurations, where the background Drude peak is not shown. For ferromagnetic order, σ_1 vanishes at nonzero frequencies in the absence of external disorder because of an effective Galilean invariance. In contrast, an antiferromagnetic order generates characteristic peaks at phonon frequencies $\omega_{L,T}(q)$ corresponding to the ordering wave vector q (purple line for stripe antiferromagnet and orange line for 120° Néel anti-ferromagnetism), which is a direct spectroscopic signature for experimental identification. In a spin liquid phase (blue line), the conductivity spectrum closely resembles the phononic density of states. We used the carrier density $n = 10^{11} \text{ cm}^{-2}$, the effective mass $m = 0.5m_e$ and Berry curvature $\Omega = 10 \text{ \AA}^2$ motivated by those in monolayer MoSe₂ [7, 8], and the phononic damping rate $\gamma = 0.1 \text{ THz}$.

remains unchanged. As a result, the optical response is the same as that of an ideal metal, and cannot reveal the complicated single electron band structure [37] of a Wigner crystal unless there is pinning from disorder [38–41] or moiré potential, see End Matter for details of pinning. Indeed, the zero g limit of Eq. (5) yields $\mathbf{u}^{(0)} = -\mathcal{E}/\omega^2$ considering that the dynamical matrix $\hat{\phi}$ satisfies $\hat{\phi} \mathcal{E} \propto \sum_j \hat{\phi}_{ij} = 0$ because of translational invariance. This corresponds to the optical conductivity $\sigma = ine^2/(m\omega)$. Note that translational invariance is enough to constrain the coupling of uniform external field to the $q = 0$ phonon only, so that there is only Drude response with a pole at zero frequency. However, Galilean invariance provides a further constraint that, this linear response is already exact and there are no nonlinear responses.

With the site-dependent Berry curvature $\hat{g}_i = m\Omega_i \hat{\epsilon}$ that breaks the Galilean invariance via the anomalous velocity, the motions of the electrons are no longer perfectly synchronized, as shown in Fig. 1(a). As a result, the driven dynam-

ics may distort the crystal, leading to nontrivial excitations of the phonons at nonzero momenta. This effect must manifest as absorption peaks in the optical conductivity. Since the anomalous-velocity effect in TMDCs is weak, we perform a perturbative expansion in Ω to resolve its impact on the optical response. From Eq. (5), the first order Berry curvature correction to the displacement is $\mathbf{u}^{(1)} = \hat{G}(\omega)i\omega\hat{g}\mathcal{E}$. Its momentum- q component reads

$$\mathbf{u}_q^{(1)} = \sum_{\alpha} \frac{i\omega\mathbf{v}_{\alpha,q}}{\omega_{\alpha,q}^2 - \omega^2 - i\gamma\omega} [\mathbf{v}_{\alpha,q}\hat{g}(q)\mathcal{E}] \quad (6)$$

where we have added a nonzero damping rate γ for the phonons. The momentum summation \sum_q is over the N momenta in the first Brillouin zone, and goes to the dimensionless integral $\frac{N}{V_B} \int d^2q$ in the large system limit where the momentum volume of the first Brillouin zone is $V_B = 8\pi^2/(\sqrt{3}a^2)$ for the triangular lattice shown in Fig. 1. This correction means forced phononic oscillations at nonzero momenta q and frequency ω . They exist because the uniform driving field \mathcal{E} gains a coupling to the momentum- q phonon via $\hat{g}(q) = \frac{1}{N} \sum_i e^{-i\mathbf{q}\cdot\mathbf{R}_i} \hat{g}_i = m\Omega\hat{E}S_q^z$, the q component of the pseudospin as shown in Fig. 1(a), similar to disorder effect.

The zero momentum component of $\mathbf{u}^{(1)}$ satisfies $\mathcal{E} \cdot \mathbf{u}^{(1)} = 0$, meaning it is perpendicular to the applied electric field and does not contribute to the longitudinal optical conductivity σ_{xx} . However, the first-order lattice deformation generates an internal field via the elastic Coulomb kernel $\hat{\phi}$, which drives an additional anomalous-velocity response as the second-order correction $\mathbf{u}^{(2)} = -\hat{G}(\omega)i\omega\hat{g}\hat{\phi}\hat{G}(\omega)i\omega\hat{g}\mathcal{E}$, in which the q and $-q$ components from the two \hat{g} operators may combine to give a nonzero uniform displacement. Assuming the driving electric field is along x , the resulting second order uniform displacement in the x direction reads

$$u_0^{x(2)} = m^2\Omega^2 \sum_{\alpha q} \chi_q |v_{\alpha,q}^y|^2 \frac{\omega_{\alpha,q}^2}{\omega^2 + i\gamma\omega - \omega_{\alpha,q}^2} \mathcal{E}, \quad (7)$$

see End Matter for detailed derivation. Plugging it into the current $\mathbf{J} = ne\dot{\mathbf{u}}$, one obtains the $O(\Omega^2)$ contribution to the longitudinal optical conductivity along the x -direction:

$$\sigma(\omega) = ne^2 m\Omega^2 \sum_{\alpha q} \chi_q |v_{\alpha,q}^y|^2 \frac{i\omega\omega_{\alpha,q}^2}{\omega^2 + i\gamma\omega - \omega_{\alpha,q}^2}. \quad (8)$$

It is now manifest that the Berry curvature spatial disorder (such as that in a pseudospin liquid state) breaks Galilean invariance via the anomalous velocity, engaging phonons at nonzero momenta and introducing absorption peaks to the optical response. Crucially, a z -pseudospin long range order at nonzero momentum q_0 , characterized by a delta-function peak in χ_q , will generate sharp peaks in the optical absorption at the phonon frequencies corresponding to the same q_0 , see Fig. 1(b). This connection provides a direct optical spectroscopic method for detecting pseudospin orders.

The optical conductivity spectra of the representative states are shown in Fig. 1(c). The ferromagnetic long range order with uniform pseudospin alignment corresponds to $\chi_q =$

$\frac{V_B}{N} \delta(q)$ at the mean field level, which exhibits no nonzero frequency peaks in σ according to Eq. (8). Therefore, it is indistinguishable from the case without Berry curvature effects. On the other hand, the stripe AFM state has $\chi_q = \frac{V_B}{N} \delta(q - q_0)$, leading to two sharp peaks at the phonon frequencies ω_{L,q_0} and ω_{T,q_0} . There is only one peak in Fig. 1(c) because the transverse phonon has zero $u_{T,q}^y$ for the $q_0 \parallel \hat{y}$ used there. We used the true long-range ordered state for stripe AFM for latter convenience. It will be shown to be stabilized by an Ising-type of interaction generated by optical driving. For the 120° Néel antiferromagnetic order whose ordering momenta q_K are at the K points, we use $\chi_q = \frac{V_B}{N} \sqrt{a} |q - q_K|^{-3/2} / 4\pi$ to capture the algebraic decay of s_z fluctuations in an antiferromagnetic Heisenberg model [42, 43]. Note that this is a result after averaging all possible orientations of the 120° order. For the spin liquid and the trivial paramagnetic phases, the short-range correlation with the decay length ξ is captured by a weak momentum dependence: $\chi_q = \frac{V_B}{N} a^2 \left[\sqrt{1/a^2 + 1/\xi^2} + 1/\xi \right] (q^2 + 1/\xi^2)^{-1/2} / 2\pi$ [42]. Therefore, its optical absorption spectrum roughly reflects the phononic density of states.

Optical Manipulation— We now proceed to show that, in addition to optical detection of equilibrium pseudospin orders, the same Berry curvature effect also enables optical manipulation of pseudospin orders under strong THz field. This phenomenon arises from the ponderomotive potential, the effective static potential generated by the driving field on the low energy degrees of freedom [36]. In the Wigner crystal of interest, the natural low energy degrees of freedom are the pseudospins. Their typical excitation energy scale is set by the ferromagnetic exchange coupling $J \sim \mu\text{eV}$ [16] which is much lower than the THz frequency of the driving field and the phonon frequency in Fig. 1(b).

Before the derivation, one may glean physical insights into the light induced potential $V_P(S_i)$ on the pseudospin directly from the equilibrium optical response in Eq. (8). The latter shows that the pseudospin wave χ_q at momentum q contributes a Lorentzian pole at frequency $\omega_{\alpha,q}$ to the optical conductivity. In certain cases [36], the ponderomotive potential induced by the linearly polarized driving electrical field $2E \cos(\omega t)$ is given by $V_P(S_i) = E^2 \text{Im}[\sigma(\omega, S_i)] / \omega$ to lowest order in the field strength. This potential is negative for the pseudospin waves whose corresponding phonon frequencies $\omega_{\alpha,q}$ are higher than the driving frequency ω . Therefore, the optical drive tends to push these pseudospin waves to higher values. In other words, it will favor certain pseudospin orders, especially the stripe AFM state at the momentum q whose $\omega_{\alpha,q}$ is slightly above the driving frequency. In case the relation of the ponderomotive potential to the optical conductivity is not rigorous, we derive the former directly from the equation of motion in the following.

Formally, the total Lagrangian of the Wigner crystal is $L = L_f + L_s$ where L_f is from Eq. (1). The pseudospin part of the lagrangian is obtained from the spin-coherent-state path integral representation of the spin Hamiltonian $H_0(\mathcal{S})$ as $L_s = -\sum_i \mathcal{A}(\mathbf{S}_i) \cdot \dot{\mathbf{S}}_i + H_0(\mathbf{S})$. Here the first term is the

Berry phase term where $\nabla_s \times \mathcal{A}(\mathbf{S}) = \hat{S}$ and should be distinguished from the electronic Berry connection in Eq. (1). The force exerted by the driven phonons on the classical spin \mathbf{S} is $F_i = -\partial_{S_i} L_f = \Omega k_i^x k_i^y$ which is purely along the S_z direction, see Eq. (1). On the classical mean field level, its time average is the ponderomotive force [36]:

$$F_{Pi} = \Omega \langle k_i^x k_i^y \rangle_t, \quad F_P(q) = \sum_i e^{-i\mathbf{q} \cdot \mathbf{R}_i} F_{Pi} = NC_q S_q^z, \\ C_q = E^2 m e^2 \Omega^2 \sum_{\alpha} |u_{\alpha,q}^y|^2 \text{Re} \left[\frac{\omega_{\alpha q}^2}{\omega_{\alpha q}^2 - \omega^2 - i\gamma\omega} \right], \quad (9)$$

see Appendix B for a derivation. Here $F_P(q)$ is the force felt by \mathbf{S}_{-q} , the momentum- q component of the spin configuration, expanded to lowest order in the Berry curvature Ω . The k_i^x and k_i^y are found from Eq. (6) and the equation of motion relating \mathbf{u} and \mathbf{k} . Note that because the model in Eq. (1) is quadratic in the electronic displacements and momenta, there is only linear response of the phonons to the driving field but no nonlinear responses. Therefore, the $O(E^2)$ ponderomotive force in Eq. (9) is already an exact expansion in the driving field and there are no higher order corrections. The quantum and thermal fluctuation corrections to the force could be obtained by changing the time-average to the Keldysh path integral $F_{Pi} = -\langle \partial_{S_i} L_f \rangle_{\text{path integral}}$ [36, 44], which is beyond the scope of this work.

Integrating the force over \mathbf{S}_q , one obtains the ponderomotive potential V_P from Eq. (9), which renders the net effective pseudospin Hamiltonian

$$H_{\text{eff}} = -J \sum_{\langle ij \rangle} \hat{s}_i \cdot \hat{s}_j + V_P, \quad V_P = -N \sum_q C_q \hat{s}_{-q}^z \hat{s}_q^z. \quad (10)$$

Here the first term is a nearest neighbor Heisenberg ferromagnetic coupling that roughly accounts for the equilibrium exchange coupling and ring exchange effects [14, 15, 17, 19–21] and $\langle ij \rangle$ means nearest neighbor. The second term is the ponderomotive potential generated by the optical drive, which could also be written in real space as $V_P = -\sum_{ij} J_{ij} \hat{s}_i^z \hat{s}_j^z$ where $J_{ij} = \frac{1}{N} \sum_q C_q e^{i\mathbf{q} \cdot (\mathbf{R}_i - \mathbf{R}_j)}$ is a nonlocal Ising type of coupling. Note that it is exactly the formula $V_P(S_i) = E^2 \text{Im}[\sigma(\omega, S_i)]/\omega$ predicted by the optical conductivity since $\chi_q = S_{-q}^z S_q^z$ in Eq. (8). From Eq. (9), C_q is maximized for $\omega_{\alpha q}$ closely above ω , meaning that the ponderomotive potential favors the pseudospin order with the momentum q whose corresponding phonon frequency is closely above the driving frequency.

Next, we employ a variational approach to analyze its phase diagram within the mean-field level. The variational wave function for the stripe AFM state with long range valley-pseudospin order at momentum q is

$$|q\rangle = \prod_i \exp\left(i \frac{\sigma_y}{2} \mathbf{q} \cdot \mathbf{R}_i\right) |\uparrow\rangle_i \quad (11)$$

where $|\uparrow\rangle_i$ means the pseudospin-up state with $s^z = 1$ at site i , see Fig. 2(a) for an illustration. The energy per site of this

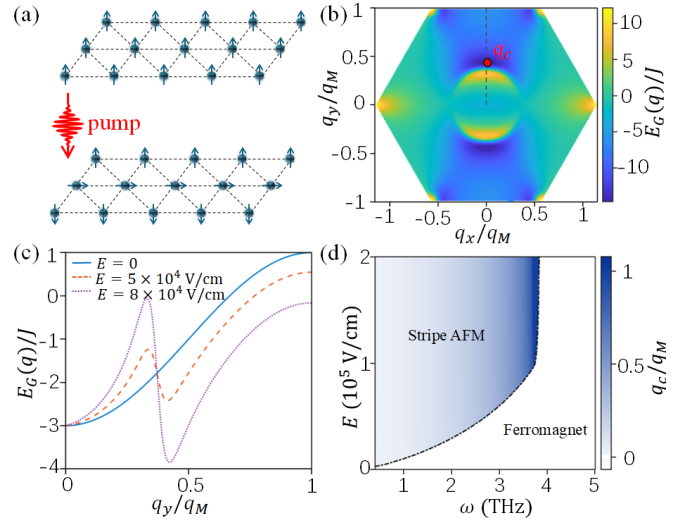


FIG. 2. Light manipulated pseudospin order. (a) Schematic illustration of the pump light switching the ferromagnetic Wigner crystal to a strip antiferromagnetic state. (b) The energy landscape $E_G(q)$ of the stripe antiferromagnetic state as a function of its ordering momentum \mathbf{q} (in units of $q_M = 2\pi/(\sqrt{3}a)$) under the x -polarized driving field $E = 2 \times 10^5$ V/cm at the driving frequency $\omega = 3.1$ THz. The global energy minimum corresponds to the optimized ordering momentum which locates along the q_y direction. (c) Cross-sectional cuts of $E_G(q)$ along the gray line in (b) for three different pump fields, showcasing the pump induced phase transition. (d) The zero temperature phase diagram on the plane of driving frequency ω and electric field E , with the color scale encoding the pseudospin ordering wave vector q_y . The gray dashed line marks the critical field E_c required to drive the phase transition. The other parameters used are $\gamma = 0.3$ THz, $n = 10^{11}$ cm $^{-2}$, $J = 5$ μ eV and $\Omega = 10$ \AA^2 , consistent with those in MoSe $_2$ [7, 8].

state is

$$E_G(q) = \frac{1}{N} \langle q | H_{\text{eff}} | q \rangle = -\frac{1}{2} J \sum_{m=1}^6 \cos(\mathbf{q} \cdot \mathbf{a}_m) - \frac{1}{2} C_q \quad (12)$$

where \mathbf{a}_m are the six real space vectors pointing from a site to its six nearest neighbors on the triangular lattice. In the absence of the driving field E , the energy is minimized by $q = 0$ corresponding to ferromagnetic order.

The optical drive induces the ponderomotive potential $-C_q$ that favors the pseudospin orders with $\omega_{\alpha q} > \omega$. From the Lorentzian structure of $-C_q$ in Eq. (9), with fixed $\alpha = \text{L}$ or T , it has a sharp minimum at q_c satisfying $\omega_{\alpha q_c} - \omega \sim \gamma$. This creates a new minimum in the total energy at roughly the same momentum, as plotted in Fig. 2(b)(c). Therefore, for strong enough driving field, the new minimum becomes lower than that at zero momentum, so that the global minimum is the stripe antiferromagnetic state $|q_c\rangle$. The phase diagram is presented in Fig. 2(d) on the plane of the driving frequency and field. As the driving field is tuned beyond the threshold $E_c(\omega)$, the system undergoes a first-order phase transition from the ferromagnetic state $|0\rangle$ into the stripe antiferromagnetic state $|q_c\rangle$. The threshold could be estimated as $E_c(\omega) \sim (J\gamma a^2 \omega^3 m / \Omega^2 n^2 e^6)^{1/2}$ for $\omega \ll W$ and $E_c(\omega) \sim (J\gamma / \Omega^2 m e^2 \omega)^{1/2}$ for $\omega \approx W$

where W is the phononic bandwidth of the Wigner crystal. Notably, as the driving frequency approaches $W = 3.8$ THz, the ordering wave vector $q_c = q_M$ reaches the M point at the Brillouin zone boundary, corresponding to the stripe antiferromagnetic state in the inset of Fig. 1(c).

The light-induced stripe AFM state is an Ising type of order that spontaneously breaks the translational symmetry and the Z_2 symmetry of $S_z \rightarrow -S_z$. If the favored wave vector q_c is commensurate with the underlying electronic lattice, the broken symmetry is discrete and this phase will be stable below a nonzero critical temperature set roughly by $T_c \sim C_{q_c}$. For the driving frequency $\omega = 3.8$ THz so that $q_c = q_M$ and at the driving field $E = 3 \times 10^5$ V/cm, this temperature is estimated to be $T_c \sim 3$ K for TMDC monolayers with the parameters in Fig. 2. In TMDC moiré structures where the typical Berry curvature of the lowest electronic bands is ~ 100 times larger [45] because of much smaller Brillouin zones, the critical temperature is boosted to $T_c \sim 13$ K for an even weaker driving field $E = 6 \times 10^3$ V/cm. If the favored wave vector is incommensurate and if the continuous rotational symmetry around S_z is also broken, the fluctuations are stronger and will be addressed by future research.

Note that the optical drive injects heat into the system by exciting the electronic phonons, which is already included in our calculation. Within our model, we assume that the heat does not accumulate but is dissipated into the environment through the nonzero damping rate γ of the phonons. In principle, the effective temperature for the low energy pseudospin model in Eq. (10) is encoded in the noise and friction the pseudospins experience, which do have contributions from the optical drive. This effect is left for future research.

Discussion— So far, we have focused on the center-of-mass motion of each electron at the classical level, such that only the z-direction pseudospin S^z affects its equation of motion from Eq. (1). However, we note that if the pseudospin is purely along S^x or S^y direction, it may be viewed as a quantum superposition of $S^z = 1$ and $S^z = -1$ states. In this case, the anomalous velocity under external field splits the electron into two wave packets moving in opposite directions, stretching it without changing the center of mass. This stretching motion constitutes a quantum mechanical correction to the optical response. It may be roughly accounted for by a local quantum fluctuation of z-pseudospin as $\chi_{ij}^{\text{quantum}} = \langle S_i^z S_j^z \rangle = \delta_{ij}$ plugged into Eq. (8). Therefore, this effect contributes an incoherent background to the optical absorption, which should not mask the sharp peaks of the long range AFM orders of z-pseudospin or the light induced ponderomotive potential in Eq. (10).

In conclusion, we have theoretically predicted that pseudospin orders can be detected and manipulated in Wigner crystals using THz optics. One promising experimental direction is to write the stripe AFM order using a THz optical pulse and read it with a second THz pulse, demonstrating an ultrafast memory. Beyond this prototypical example, our work also sheds light on the efficient optical control of spin/pseudospin manybody states in generic systems via spin-orbit coupling, pushing the optical engineering of nonequilibrium matter [46–

48] towards correlated states [49, 50].

We thank I. Esterlis, M. M. Fogler, H. Park and S. Zhou for helpful discussions. Y.D. and Z.S. acknowledge support from the National Natural Science Foundation of China (Grants No. 12421004 and No. 12374291), Beijing Natural Science Foundation (Z240005), and the startup grant from Tsinghua University. E.D. acknowledges support from the SNSF project 200021_212899, and NCCR SPIN, a National Centre of Competence in Research, funded by the Swiss National Science Foundation (grant number 225153).

* Corresponding author: zysun@tsinghua.edu.cn

† Corresponding author: demlere@ethz.ch

-
- [1] E. Wigner, On the Interaction of Electrons in Metals, *Physical Review* **46**, 1002 (1934).
 - [2] L. Bonsall and A. A. Maradudin, Some static and dynamical properties of a two-dimensional Wigner crystal, *Physical Review B* **15**, 1959 (1977).
 - [3] Y. Zhou, I. Esterlis, and T. Smoleski, *Electronic crystals in layered materials* (2025), arXiv:2509.21222 [cond-mat.str-el].
 - [4] Y. E. Lozovik and V. I. Yudson, Crystallization of a two-dimensional electron gas in a magnetic field, *Soviet Journal of Experimental and Theoretical Physics Letters* **22**, 11 (1975).
 - [5] C. C. Grimes and G. Adams, Evidence for a liquid-to-crystal phase transition in a classical, two-dimensional sheet of electrons, *Phys. Rev. Lett.* **42**, 795 (1979).
 - [6] J. Yoon, C. C. Li, D. Shahar, D. C. Tsui, and M. Shayegan, Wigner crystallization and metal-insulator transition of two-dimensional holes in GaAs at $B = 0$, *Phys. Rev. Lett.* **82**, 1744 (1999).
 - [7] T. Smoleski, P. E. Dolgirev, C. Kuhlenkamp, A. Popert, Y. Shimazaki, P. Back, X. Lu, M. Kroner, K. Watanabe, T. Taniguchi, I. Esterlis, E. Demler, and A. Imamolu, Signatures of Wigner crystal of electrons in a monolayer semiconductor, *Nature* **595**, 53 (2021).
 - [8] Y. Zhou, J. Sung, E. Brutschea, I. Esterlis, Y. Wang, G. Scuri, R. J. Gelly, H. Heo, T. Taniguchi, K. Watanabe, G. Zaránd, M. D. Lukin, P. Kim, E. Demler, and H. Park, Bilayer Wigner crystals in a transition metal dichalcogenide heterostructure, *Nature* **595**, 48 (2021).
 - [9] J. Sung, J. Wang, I. Esterlis, P. A. Volkov, G. Scuri, Y. Zhou, E. Brutschea, T. Taniguchi, K. Watanabe, Y. Yang, M. A. Morales, S. Zhang, A. J. Millis, M. D. Lukin, P. Kim, E. Demler, and H. Park, An electronic microemulsion phase emerging from a quantum crystal-to-liquid transition, *Nature Physics* **21**, 437 (2025).
 - [10] Z. Xiang, H. Li, J. Xiao, M. H. Naik, Z. Ge, Z. He, S. Chen, J. Nie, S. Li, Y. Jiang, R. Sailer, R. Banerjee, T. Taniguchi, K. Watanabe, S. Tongay, S. G. Louie, M. F. Crommie, and F. Wang, Imaging quantum melting in a disordered 2D Wigner solid, *Science* **388**, 736 (2025).
 - [11] Y.-C. Tsui, M. He, Y. Hu, E. Lake, T. Wang, K. Watanabe, T. Taniguchi, M. P. Zaletel, and A. Yazdani, Direct observation of a magnetic-field-induced Wigner crystal, *Nature* **628**, 287 (2024).
 - [12] E. C. Regan, D. Wang, C. Jin, M. I. Bakti Utama, B. Gao, X. Wei, S. Zhao, W. Zhao, Z. Zhang, K. Yumigeta, M. Blei, J. D. Carlström, K. Watanabe, T. Taniguchi, S. Tongay, M. Crommie, A. Zettl, and F. Wang, Mott and generalized

- Wigner crystal states in WSe₂/WS₂ moiré superlattices, *Nature* **579**, 359 (2020).
- [13] H. Li, S. Li, E. C. Regan, D. Wang, W. Zhao, S. Kahn, K. Yumigeta, M. Blei, T. Taniguchi, K. Watanabe, S. Tongay, A. Zettl, M. F. Crommie, and F. Wang, Imaging two-dimensional generalized Wigner crystals, *Nature* **597**, 650 (2021).
- [14] B. Bernu, L. Cândido, and D. M. Ceperley, Exchange frequencies in the 2d wigner crystal, *Phys. Rev. Lett.* **86**, 870 (2001).
- [15] N. D. Drummond and R. J. Needs, Phase Diagram of the Low-Density Two-Dimensional Homogeneous Electron Gas, *Physical Review Letters* **102**, 126402 (2009).
- [16] J. Knörzer, M. J. A. Schuetz, G. Giedke, D. S. Wild, K. De Greve, R. Schmidt, M. D. Lukin, and J. I. Cirac, Wigner crystals in two-dimensional transition-metal dichalcogenides: Spin physics and readout, *Physical Review B* **101**, 125101 (2020).
- [17] K.-S. Kim, C. Murthy, A. Pandey, and S. A. Kivelson, Interstitial-induced ferromagnetism in a two-dimensional wigner crystal, *Phys. Rev. Lett.* **129**, 227202 (2022).
- [18] V. Calvera, S. A. Kivelson, and E. Berg, Pseudo-spin order of Wigner crystals in multi-valley electron gases, *Low Temperature Physics* **49**, 679 (2023).
- [19] K.-S. Kim, I. Esterlis, C. Murthy, and S. A. Kivelson, Dynamical defects in a two-dimensional wigner crystal: Self-doping and kinetic magnetism, *Phys. Rev. B* **109**, 235130 (2024).
- [20] I. Esterlis, D. Zverevich, Z. Zhuang, and A. Levchenko, Magnetism of the bilayer wigner crystal, *Phys. Rev. B* **111**, 075159 (2025).
- [21] I. Esterlis and A. Levchenko, Magnetism from multiparticle ring exchange in moiré wigner crystals, *Phys. Rev. B* **111**, L201115 (2025).
- [22] M. S. Hossain, M. K. Ma, K. A. V. Rosales, Y. J. Chung, L. N. Pfeiffer, K. W. West, K. W. Baldwin, and M. Shayegan, Observation of spontaneous ferromagnetism in a two-dimensional electron system, *Proceedings of the National Academy of Sciences* **117**, 32244 (2020).
- [23] J. Falson, I. Sodemann, B. Skinner, D. Tabrea, Y. Kozuka, A. Tsukazaki, M. Kawasaki, K. von Klitzing, and J. H. Smet, Competing correlated states around the zero-field wigner crystallization transition of electrons in two dimensions, *Nature Materials* **21**, 311 (2022).
- [24] M. Zarenia, D. Neilson, B. Partoens, and F. M. Peeters, Wigner crystallization in transition metal dichalcogenides: A new approach to correlation energy, *Physical Review B* **95**, 115438 (2017).
- [25] Z. Lu, T. Han, Y. Yao, Z. Hadjri, J. Yang, J. Seo, L. Shi, S. Ye, K. Watanabe, T. Taniguchi, and L. Ju, Extended quantum anomalous hall states in graphene/hbn moiré superlattices, *Nature* **637**, 1090 (2025).
- [26] J. Dong, T. Wang, T. Wang, T. Soejima, M. P. Zaletel, A. Vishwanath, and D. E. Parker, Anomalous hall crystals in rhombohedral multilayer graphene. i. interaction-driven chern bands and fractional quantum hall states at zero magnetic field, *Phys. Rev. Lett.* **133**, 206503 (2024).
- [27] T. Tan and T. Devakul, Parent berry curvature and the ideal anomalous hall crystal, *Phys. Rev. X* **14**, 041040 (2024).
- [28] Y. Zeng, D. Guerci, V. Crépel, A. J. Millis, and J. Cano, Sublattice structure and topology in spontaneously crystallized electronic states, *Phys. Rev. Lett.* **132**, 236601 (2024).
- [29] T. Soejima, J. Dong, T. Wang, T. Wang, M. P. Zaletel, A. Vishwanath, and D. E. Parker, Anomalous hall crystals in rhombohedral multilayer graphene. ii. general mechanism and a minimal model, *Phys. Rev. B* **110**, 205124 (2024).
- [30] Z. Dong, A. S. Patri, and T. Senthil, Stability of anomalous hall crystals in multilayer rhombohedral graphene, *Phys. Rev. B* **110**, 205130 (2024).
- [31] D. Xiao, G.-B. Liu, W. Feng, X. Xu, and W. Yao, Coupled Spin and Valley Physics in Monolayers of MoS₂ and Other Group-VI Dichalcogenides, *Physical Review Letters* **108**, 196802 (2012).
- [32] X. Xu, W. Yao, D. Xiao, and T. F. Heinz, Spin and pseudospins in layered transition metal dichalcogenides, *Nature Physics* **10**, 343 (2014).
- [33] S. Manzeli, D. Ovchinnikov, D. Pasquier, O. V. Yazyev, and A. Kis, 2D transition metal dichalcogenides, *Nature Reviews Materials* **2**, 1 (2017).
- [34] D. Xiao, M.-C. Chang, and Q. Niu, Berry phase effects on electronic properties, *Rev. Mod. Phys.* **82**, 1959 (2010).
- [35] J. Dong, O. E. Sommer, T. Soejima, D. E. Parker, and A. Vishwanath, Phonons in electron crystals with berry curvature, *Proceedings of the National Academy of Sciences* **122**, e2515532122 (2025).
- [36] Z. Sun, Floquet engineering of many-body states by the ponderomotive potential, *Physical Review B* **110**, 104301 (2024).
- [37] S. Brem and E. Malic, Terahertz Fingerprint of Monolayer Wigner Crystals, *Nano Letters* **22**, 1311 (2022).
- [38] M. M. Fogler and D. A. Huse, Dynamical response of a pinned two-dimensional Wigner crystal, *Physical Review B* **62**, 7553 (2000).
- [39] R. Chitra, T. Giamarchi, and P. Le Doussal, Pinned wigner crystals, *Phys. Rev. B* **65**, 035312 (2001).
- [40] R. Chitra and T. Giamarchi, Zero field wigner crystal, *The European Physical Journal B - Condensed Matter and Complex Systems* **44**, 455 (2005).
- [41] P. E. Dolgirev, I. Esterlis, A. A. Zibrov, M. D. Lukin, T. Giamarchi, and E. Demler, Local noise spectroscopy of wigner crystals in two-dimensional materials, *Phys. Rev. Lett.* **132**, 246504 (2024).
- [42] W.-J. Hu, S.-S. Gong, W. Zhu, and D. N. Sheng, Competing spin-liquid states in the spin-1/2 Heisenberg model on the triangular lattice, *Physical Review B* **92**, 140403 (2015).
- [43] T. Jolicoeur, E. Dagotto, E. Gagliano, and S. Bacci, Ground-state properties of the S=1/2 Heisenberg antiferromagnet on a triangular lattice, *Physical Review B* **42**, 4800 (1990).
- [44] T. Huang and Z. Sun, Universal phase transitions of matter induced in optically driven cavities (2025), [arXiv:2505.24318 \[cond-mat.mes-hall\]](https://arxiv.org/abs/2505.24318).
- [45] F. Wu, T. Lovorn, E. Tutuc, I. Martin, and A. H. MacDonald, Topological insulators in twisted transition metal dichalcogenide homobilayers, *Phys. Rev. Lett.* **122**, 086402 (2019).
- [46] C. Bao, P. Tang, D. Sun, and S. Zhou, Light-induced emergent phenomena in 2D materials and topological materials, *Nature Reviews Physics* **4**, 33 (2022).
- [47] T. Mori, Floquet States in Open Quantum Systems, *Annual Review of Condensed Matter Physics* **14**, 35 (2023).
- [48] M. S. Rudner and N. H. Lindner, Band structure engineering and non-equilibrium dynamics in Floquet topological insulators, *Nature Reviews Physics* **2**, 229 (2020).
- [49] A. de la Torre, D. M. Kennes, M. Claassen, S. Gerber, J. W. McIver, and M. A. Sentef, Colloquium: Nonthermal pathways to ultrafast control in quantum materials, *Rev. Mod. Phys.* **93**, 041002 (2021).
- [50] Y. Murakami, D. Golež, M. Eckstein, and P. Werner, Photoinduced nonequilibrium states in mott insulators, *Rev. Mod. Phys.* **97**, 035001 (2025).
- [51] D. Xiao, W. Yao, and Q. Niu, Valley-Contrasting Physics in Graphene: Magnetic Moment and Topological Transport, *Physical Review Letters* **99**, 236809 (2007).

End Matter

Appendix A: Derivation of the optical conductivity— In this section, we expand Eq. (5) for the electronic displacement to 2nd-order in Ω which yields Eq. (7) and Eq. (8), the Berry curvature correction to the longitudinal conductivity of the Wigner crystal. Note that strictly speaking, \mathbf{u} in Eq. (5) is a $2N$ component vector for all the displacements, while $\hat{g} = m\Omega_1\hat{e}_1 \oplus m\Omega_2\hat{e}_2 \oplus \dots \oplus m\Omega_N\hat{e}_N$ and $\hat{\phi}$ are viewed as $2N \times 2N$ matrices. Later on, these notations are also used with the lattice indices removed. However, this shouldn't cause a misunderstanding.

The 0th-order term involves the contribution from the Γ -point phonon only:

$$\mathbf{u}^{(0)} = \hat{G}(\omega)\mathcal{E} = -\mathcal{E}/\omega^2. \quad (\text{A1})$$

Consequently, the optical conductivity corresponding to this term exhibits a Drude conductivity.

The 1st-order term in Eq. (6) is straightforward to derive from expanding Eq. (5). There are two terms that may contribute: the anomalous velocity response to the external field, and that to the internal electric field generated by 0th-order motion. However, the latter is zero because $\hat{\phi}^{\mathcal{E}} = 0$, i.e., the 0th-order motion corresponds to uniform displacement of the lattice and induces no internal field. The former term reads

$$\mathbf{u}^{(1)} = \hat{G}(\omega)i\omega\hat{g}^{\mathcal{E}} = \sum_{\alpha q} \frac{i\omega}{\omega_{\alpha,q}^2 - \omega^2} \tilde{v}_{\alpha,q} \tilde{v}_{\alpha,q}^T \hat{g}^{\mathcal{E}} \quad (\text{A2})$$

where we inserted the complete basis $\hat{I} = \sum_{\alpha q} \tilde{v}_{\alpha,q} \tilde{v}_{\alpha,q}^T$. Writing out the lattice index explicitly and focusing on the Fourier component at q , one obtains Eq. (6).

The 2nd-order term arises from the anomalous velocity generated from the lattice potential induced by the 1st-order deformations. Expanding Eq. (5) to $O(\hat{g}^2)$ and making use of $\hat{\phi}^{\mathcal{E}} = 0$ again, one obtains

$$\begin{aligned} \mathbf{u}^{(2)} &= -\hat{G}(\omega)i\omega\hat{g}\hat{\phi}\hat{G}(\omega)i\omega\hat{g}^{\mathcal{E}} \\ &= \omega^2 \sum_{\beta q', \alpha q} \frac{\tilde{v}_{\beta,q'} \tilde{v}_{\beta,q'}^T}{\omega_{\beta,q'}^2 - \omega^2} \hat{g} \omega_{\alpha,q}^2 \frac{\tilde{v}_{\alpha,q} \tilde{v}_{\alpha,q}^T}{\omega_{\alpha,q}^2 - \omega^2} \hat{g}^{\mathcal{E}}. \end{aligned} \quad (\text{A3})$$

Selecting $q' = 0$ component, one obtains the zero-momentum displacement

$$\mathbf{u}_0^{(2)} = \sum_{\alpha\beta q} \frac{m^2\Omega^2\chi_{\alpha,q}\omega_{\alpha,q}^2}{\omega^2 + i\gamma\omega - \omega_{\alpha,q}^2} \mathbf{v}_{\beta,0} (\mathbf{v}_{\beta,0}\hat{e}\mathbf{v}_{\alpha,q}) (\mathbf{v}_{\alpha,q}\hat{e}\mathcal{E}) \quad (\text{A4})$$

where a phenomenological damping rate γ has been added. Focusing on the driving field along x , one obtains Eq. (7) and Eq. (8).

Appendix B: Derivation of the ponderomotive force— In this section, we derive the expression for the ponderomotive force acting on \mathbf{S}_q given by Eq. (9). The ponderomotive force experienced by the i -th electron is given by $F_{Pi} = \Omega\langle k_i^x k_i^y \rangle_t$,

where k_i^x and k_i^y could be found from the Hamilton equation of motion

$$k_i^x = \dot{u}_i^x - m\Omega k_i, \quad k_i^y = -[\hat{\phi}\mathbf{u}]_i^y \quad (\text{B1})$$

for the driving field is along the x direction. The displacement \mathbf{u} could be found from (A1) and (A2). Because $\mathbf{u}^{(0)}$ is the uniform motion of electron lattice, it satisfies $\hat{\phi}\mathbf{u}^{(0)} = 0$. Thus the leading order result for $k^y(q) = \frac{1}{N} \sum_i e^{-i\mathbf{q}\cdot\mathbf{R}_i} k_i^y$ comes from the $\mathbf{u}^{(1)}$ term in Eq. (6):

$$-i\omega k^y(q, \omega) = \sum_{\alpha} \frac{-i\omega\omega_{\alpha,q}^2 v_{\alpha,q}^y}{\omega_{\alpha,q}^2 - \omega^2 - i\gamma\omega} [\mathbf{v}_{\alpha,q}\hat{g}(q)\mathcal{E}]. \quad (\text{B2})$$

which is $O(\Omega)$. Therefore, for the $O(\Omega^2)$ result of the ponderomotive force, one just needs the zeroth order result of k_i^x : $k_i^x(\omega) = ieE/\omega$. Plugging them in the expression $F_{Pi} = \Omega\langle k_i^x k_i^y \rangle_t$ and taking the combination between positive and negative frequency components, one obtains the ponderomotive force for the Fourier component \mathbf{S}_{-q} in Eq. (9).

Appendix C: Berry curvature in TMDCs— The effective two-band Hamiltonian for low energy electrons in monolayer TMDCs could be written as [31, 34, 51] $H = v(\tau k_x \hat{\sigma}_x + k_y \hat{\sigma}_y) + \Delta \hat{\sigma}_z$ where v , $\Delta = mv^2$ and $\tau = \pm 1$ are the asymptotic velocity, the mass, and the valley index. The Berry curvature $\Omega(\mathbf{k}) = \nabla_{\mathbf{k}} \times \langle u_n(\mathbf{k}) | i\nabla_{\mathbf{k}} | u_n(\mathbf{k}) \rangle$ of the electrons in the conduction band is [34, 51]

$$\Omega(\mathbf{k}) = -\tau \frac{v^2 \Delta}{2[\Delta^2 + v^2 k^2]^{3/2}} \hat{z} \xrightarrow{k \ll mv} -\tau \frac{v^2}{2\Delta^2} \quad (\text{B3})$$

and that for the valence band is opposite. At low densities, the typical electronic momentum in a Wigner crystal is much smaller than mv , so that the Berry curvature is approximated by the constant value in the main text.

Given the typical parameters in TMDCs, Ω falls in the range of $10 - 20 \text{ \AA}^2$ [31]. To obtain a sense of its magnitude, in an electric field of $E = 10^3 \text{ V/cm}$ with a driving frequency of $\omega = 2 \text{ THz}$, the normal velocity of the forced motion of a single electron is $v_n = 1.7 \times 10^4 \text{ m/s}$. The ratio between its anomalous velocity and the normal velocity is $v_a/v = \Omega m \omega / \hbar \sim 10^{-2}$. For TMDC moiré bilayers, the typical Berry curvature of the lowest electronic bands is ~ 100 times larger [45] so that this ratio could be larger than unity.

Appendix D: Effect of pinning— Disorder potential pins the Wigner crystal and brings a gap and broadening to the phonons [38–41]. Moreover, moiré superlattices are found to host generalized Wigner crystals whose period is commensurate with the underlying moiré lattice [12, 13]. There the phonons are naturally gapped because the Wigner crystal is pinned by the moiré lattice even without disorder. The simplest way to model the pinning effect is to add a potential

term $V_{\text{pin}} = \sum_i \omega_0^2 \mathbf{u}_i^2 / (2m)$ to the Lagrangian in Eq. (1), which could also be absorbed in the φ kernel. Therefore, the formalism in the main text remains unchanged. The phonons obtain a gap equal to the pinning frequency ω_0 . In the limit of zero Berry curvature, the Drude pole of the optical conductivity is shifted to ω_0 as revealed by the Green function at zero momentum: $\hat{G}\tilde{v}_{\alpha,0} = (\omega_0^2 - \omega^2)^{-1}\tilde{v}_{\alpha,0}$. As a result, Eqs. 7 and 8 are modified to

$$u_0^{x(2)} = \frac{m^2 \Omega^2 \omega^2}{\omega^2 + i\gamma\omega - \omega_0^2} \sum_{\alpha q} \frac{\chi_q |v_{\alpha,q}^y|^2 \omega_{\alpha,q}^2}{\omega^2 + i\gamma\omega - \omega_{\alpha,q}^2} \mathcal{E} \quad (\text{D1})$$

and

$$\sigma(\omega) = \frac{ne^2 m \Omega^2 \omega^2}{\omega^2 + i\gamma\omega - \omega_0^2} \sum_{\alpha q} \frac{\chi_q |v_{\alpha,q}^y|^2 i \omega \omega_{\alpha,q}^2}{\omega^2 + i\gamma\omega - \omega_{\alpha,q}^2}. \quad (\text{D2})$$

Therefore, the qualitative conclusions are unchanged: the pseudospin order leads to sharp absorption peaks at the phonon frequencies ω_{α,q_0} corresponding to the ordering wave vector q_0 . The peak locations and spectra weights are modified by factors at the order of $\omega_{\alpha,q_0}^2 / (\omega_{\alpha,q_0}^2 - \omega_0^2)$, which is $O(1)$ for weak pinning. Similarly, the light induced ponderomotive potential in Eq. (9) is modified by the same factor, and the phase diagram of light induced stripe AFM in Fig. 2 remains qualitatively the same.